Structural, spectroscopic, and thermodynamic characterization of ammonium oxalate monohydrate mineral using theoretical solid-state methods

Francisco Colmenero[*]

Instituto de Estructura de la Materia, CSIC, C/ Serrano, 113, 28006 Madrid, Spain

*E-mail: francisco.colmenero@iem.cfmac.csic.es; Orcid: https://orcid.org/0000-0003-3418-0735

Abstract

In this study, the structural properties, main characteristics of the Raman spectrum, and the thermodynamic properties of the ammonium oxalate monohydrate mineral oxammite, $(NH_4)_2(C_2O_4) \cdot H_2O$, were investigated in theoretical solid-state calculations based on the periodic density functional theory using plane waves and pseudopotentials. The optimized structure of oxammite agreed very well with that obtained from low temperature X-ray diffraction data by structure refinement (orthorhombic symmetry, space group $P2_12_12$; lattice parameters: $a = 8.017$ Å; $b = 10.309$ Å; $c = 3.735$ Å). The calculated structural properties, including the lattice parameters, bond lengths and angles, and X-ray powder pattern, accurately reproduced the experimental information. The Raman spectrum determined theoretically agreed with that obtained experimentally. The assignment of the Raman spectral bands significantly improved their previous empirical assignment. Thus, the assignment of a large series of bands was modified and the origins of several previously unassigned bands were found. Five bands in the experimental spectrum at $2344,\ 2161,\ 1933,\ 1902,$ and $815\ cm^{-1}$, were absent from the computed spectrum and they were identified as combination bands. The band located at $2879\ cm^{-1}$ was confirmed as an overtone. Furthermore, the theoretical calculations clearly showed that some features described as single peaks in previous experimental studies were due to the contributions of several bands. The thermodynamic properties of the oxammite mineral, including the specific heats, entropies, enthalpies, and Gibbs free energies, were determined as functions of temperature. The specific heat calculated at 323 K, $C_p = 202.3\ J \cdot K^{-1} \cdot mol^{-1}$, was in good agreement with the corresponding experimental heat capacity, $C_p = 211.7\ J \cdot K^{-1} \cdot mol^{-1}$, where the values only differed by about 4%. Finally, using the computed thermodynamic data, the thermodynamic properties of the formation of oxammite as well as the free energies and reaction constants of the reaction for its thermal decomposition were determined.

Keywords: Oxalate mineral; Oxammite; Raman spectroscopy; Theoretical solid-state method; Thermodynamic property.

1. Introduction

Oxalate minerals are widespread in nature and they may be found in animals, plants, and naturally occurring mineral assemblages [1-15]. Organic minerals are mostly formed by inorganic natural processes but they may also be produced organically via biomineralization [16]. Our knowledge and understanding of the presence and transport of organic matter in the environment may be enhanced by studying the origin and formation of these minerals [3-4]. The production of oxalic acid, citric acid, and other simple organic acids has important consequences for biogeochemical reactions and metal speciation [13-15].

The identification of oxalate-bearing minerals is extremely important because they are indicators of environmental events [17] and biological activity [16]. The existence of oxalates may serve as a signature of the pre-existence of life, so these compounds are being investigated in the context of possible biological activity on Mars [4,18-30]. Oxalic acid and its mineral salts are stable under the pressure and ultraviolet irradiation environment of the surface of Mars [18-19] and, consequently, oxalate minerals could be important in Martian geochemical processes [19]. Raman spectroscopy has been chosen as one of the main analytic techniques in the Mars 2020 and ExoMars missions [20-23] for the search of the corresponding geological and biogeological spectral signatures.

Oxalate compounds are the main components of human kidney stones [5-7] and they are also produced during the degradation of ancient paintings, sculpture, and architectural works [31-36] due to both natural and anthropological phenomena, such as climatic conditions and exposure to pollutant agents. Several ancient monuments were found to be covered by a superficial film comprising several compounds such as calcium oxalate, which has protective effects against

unfavorable environmental conditions. In fact, some ammonium salts that are structurally related to ammonium oxalate have been proposed as protective agents for calcareous stone substrates [36]. Oxalate materials are also used widely in industrial and laboratory processes [37-42]. For example, ammonium oxalate may be employed to produce hydrogen cyanide [42].

X-ray powder diffraction and Raman spectroscopy [43-46,24-30,47-48] have been employed frequently for the identification of these compounds. Oxalates are readily identified using Raman spectroscopy because the Raman spectra of most oxalate minerals are mutually exclusive [24-26]. Theoretical calculations are an invaluable tool for analyzing the results obtained using these experimental techniques because they can be employed to resolve the main uncertainties that are encountered, as shown in a previous study of the sodium oxalate mineral natroxalate [49].

In the present study, theoretical solid-state methods were used to investigate the structural, Raman spectroscopic, and thermodynamic properties of the ammonium oxalate monohydrate mineral oxammite, $(NH_4)_2(C_2O_4) \cdot H_2O$. Oxammite is known as a "cave" mineral because it is often formed in caves. Oxammite is a fundamental oxalate mineral and it has attracted much attention because it exhibits negative linear compressibility (NLC), *i.e.*, its structure expands with positive volume compression as the hydrostatic pressure increases [50]. NLC is a relatively uncommon phenomenon and it has been studied rarely in organic systems. However, NLC is a highly attractive mechanical property with many important applications in several fields, such as ultrasensitive pressure-sensing devices, artificial muscles, and next-generation body armor [51-55]. A large number of biological species are considered to make use of NLC [52-53]. The mechanical behavior of oxammite mineral was investigated using density functional theory (DFT) by Qiao *et al.* [50] with small calculation parameters, and these parameters were sufficient [56]. They showed that the NLC effect was due to the $N-H\cdots O$ hydrogen bonding present in

oxammite, which results in the anomalous high-pressure behavior of the structure along the b-axis. Materials that exhibit NLC have been investigated intensively in recent decades and although these studies focused mainly on simple inorganic compounds [50], some organic materials and metal-organic frameworks that exhibit NLC have also been considered, such as oxammite and $[NH_4][Zn(HCOO)_3]$ [57]. In the latter two cases, $N-H\cdots O$ hydrogen bonding is present in the corresponding crystal structures. Qiao *et al.* [50] also obtained X-ray diffraction and Raman spectroscopic measurements to study their pressure dependence and its relationship with the NLC, but theoretical calculations were not performed for the corresponding X-ray diffraction pattern and Raman spectrum.

The oxammite mineral crystal structure has been studied based on experimental X-ray diffraction techniques [43-46] and theoretical calculations [47,50]. However, the theoretical calculations were performed using empirical force fields [47] or first-principles DFT methods with a small kinetic cutoff and k-mesh [50]. In the present study, the oxammite mineral phase was characterized in detail by using a large cutoff and k-mesh. The calculations were conducted using the periodic DFT [58-60] based on plane waves and pseudopotentials [61]. This method has been applied with satisfactory results in previous studies [62-72,49]. The calculated unit cell structure was in very good agreement with the structure obtained experimentally [44,46] and it significantly improved that obtained previously using theoretical methods [50]. The use of these large calculation parameters is required to obtain good quality properties, especially good spectroscopic predictions [62-72,49]. The Raman spectrum of the oxammite mineral phase has been recorded experimentally [24-26,47-48], but a reliable assignment of the main bands in this spectrum is not available because it was characterized incompletely using empirical arguments. In addition, the assignments performed by Frost *el al.* [24-26] and Clark and Firth [47] were significantly different.

To the best of our knowledge, the Raman spectrum of oxammite mineral has not been studied previously using full first principles solid-state theoretical methods. However, our previous study of natroxalate mineral [49] demonstrated that these methods can provide a deeper understanding of the Raman spectrum for these minerals. Consequently, the Raman spectrum of oxammite mineral was theoretically determined in detail in the present study. In addition, the thermodynamic properties of the oxammite mineral were determined, including the specific heats, entropies, enthalpies, and Gibbs free energies. Theoretical calculations are a powerful predictive tool for determining these properties because the values computed in previous studies using theoretical techniques were found to be accurate when experimental data were available for comparison [64,66,69-72,49].

2. Methods

The DFT-D2 approach based on the Perdew–Burke–Ernzerhof functional [73] supplemented with Grimme empirical dispersion corrections [74] was used for all the computations. This approach is implemented in the CASTEP code [75-76], which is a module in the Materials Studio package [77]. The introduction of dispersion corrections was required in order to improve the description of the hydrogen bond structure within the unit cell of oxammite. The pseudopotentials employed for all the ions present in the structure of this mineral were the standard norm-conserving pseudopotentials [78] given in the CASTEP program. The atomic positions and cell parameters were determined using the Broyden–Fletcher–Goldfarb–Shanno optimization method [61,79]. The calculation parameters comprising the kinetic energy cut-off and k-point mesh [80] were selected in order to obtain computed structures and energies with good convergence. The lattice parameters and atomic locations were first optimized using an initial crystalline model based in the cell

parameters and the atomic positions given by Taylor and Sabine [46]. The structure of oxammite was then determined in more complex computations with augmented calculation parameters. The final properties were obtained by using the equilibrium structure obtained with a cut-off of 900 eV and k mesh of $3 \times 2 \times 7$ (8 k points). Using this optimized structure, we also obtained the lattice parameters, bond lengths and angles, and the X-ray powder diffraction pattern [81].

After determining the equilibrium geometry for oxammite, the linear response density functional perturbation theory [82-86] implemented in the CASTEP code was used to calculate the vibrational properties. The wavenumbers reported in this study were not scaled to correct for anharmonicity and the remaining errors from the theoretical procedure employed [87]. The vibrational Raman spectrum was obtained in the form of a table comprising the wavenumbers and intensity values for each normal mode [86]. The computed Raman spectrum was then compared with the experimental spectrum and the most intense bands were assigned by analyzing the atomic vibrational motions in the corresponding normal modes.

The thermodynamic properties of oxammite were obtained using the methods developed in our previous studies [64,66,69-72,49]. The phonon spectrum at different points in the Brillouin zone can be determined by density functional perturbation theory as second order derivatives of the total energy [83]. Several important thermodynamic quantities, such as the Gibbs free energies, enthalpies, entropies, and specific heats [88], can be evaluated in the quasi-harmonic approximation based on knowledge of the entire phonon spectrum and the corresponding phonon dispersion curves and density of states. The methods used for deriving the thermodynamic properties of formation and the Gibbs free energies of reaction were described in detail in previous studies [71,72].

The calculations were conducted by imposing orthorhombic symmetry, with space group $P2_12_12$ [44-46]. However, in order to analyze the effects of the relaxation of the symmetry constraints, the optimal geometry as well as the vibrational and thermodynamic properties were also determined without applying symmetry restrictions by performing calculations using the triclinic P1 space group and an increased k-mesh comprising 21 k points. The results were very close to those obtained in the calculations where orthorhombic symmetry was enforced.

3. Results and discussion

3.1. Crystal structure of oxammite

The crystal structure of oxammite was obtained by performing increasingly complex computations. Table 1 shows the calculated lattice parameters, volume, and density compared with the experimental values given by Taylor and Sabine [46] and Robertson [44]. The experimental data were reproduced accurately. As expected, our results were in better agreement with those obtained by Robertson [44] at a temperature of 30 K than those produced by Taylor and Sabine [46] at room temperature because the computations yielded data at a temperature of 0 K. The differences in the calculated cell volume and density compared with the experimental values given by Robertson [44] were very small (about 2%).

Table 1. Lattice parameters, volume, and density of the unit cell for the crystal structure of oxammite.

Parameter	*a* (Å)	*b* (Å)	*c* (Å)	α	β	γ	Vol. (Å^3)	Dens. (g/cm^3)
Calc.	7.992	10.294	3.670	90	90	90	301.968	1.562
Exp. [44] – 30K	8.017	10.309	3.735	90	90	90	308.687	1.528
Exp. [44] – 298 K	8.035	10.309	3.795	90	90	90	314.350	1.501
Exp. [46] – 298 K	8.035	10.309	3.795	90	90	90	314.350	1.501

The computed structure is shown in Figure 1, where views are displayed of a $2 \times 2 \times 2$ supercell from the [001], [100], and [010] directions.

The unit cell of oxammite contains isolated oxalate ($C_2O_2^{2-}$) and ammonium (NH_4^+) ions as well as water molecules. The water molecules are present in the structure as free (or crystallization) water, i.e., they are not coordinated to the oxalate or ammonium fragments but instead they are hydrogen bonded to their H and O atoms. The oxalate fragment in oxammite was determined as nonplanar, which agrees with the experimental observations [44,46]. The structure comprises two types of layers, where the first is made of oxalate fragments and water molecules, and the second is formed only of ammonium fragments.

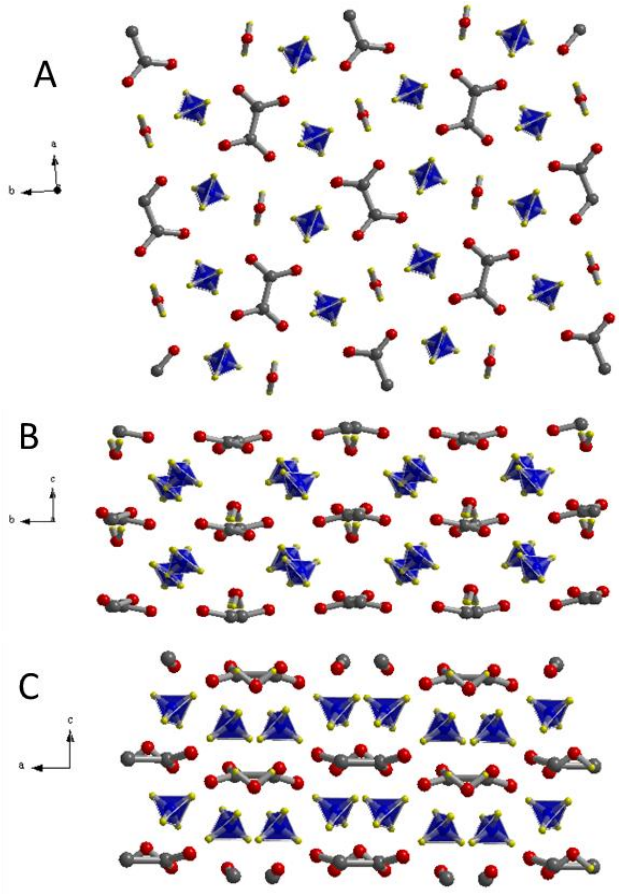

Figure 1. Structure of oxammite mineral. In this figure, a 2 × 2 × 2 supercell is shown from the [001] (A), [100] (B), and [010] (C) directions. Color code: N = blue, C = gray, O = red, H = yellow.

As shown in Figure 2, the structure of the oxammite mineral is reinforced by a dense network of hydrogen bonds. Figure 2A shows that each water molecule is the donor of two hydrogen bonds

from two oxalate fragments, and the acceptor of two hydrogen bonds from ammonium fragments. Figure 2B shows that each ammonium fragment is the donor of four hydrogen bonds, with three from oxalate fragments and one from a water molecule. Finally, Figure 2C shows the hydrogen bond structure in an oxalate fragment, where two oxygen atoms are acceptors of two hydrogen bonds from ammonium fragments and the others are acceptors of two hydrogen bonds, with one from a water molecule and the other from an ammonium fragment.

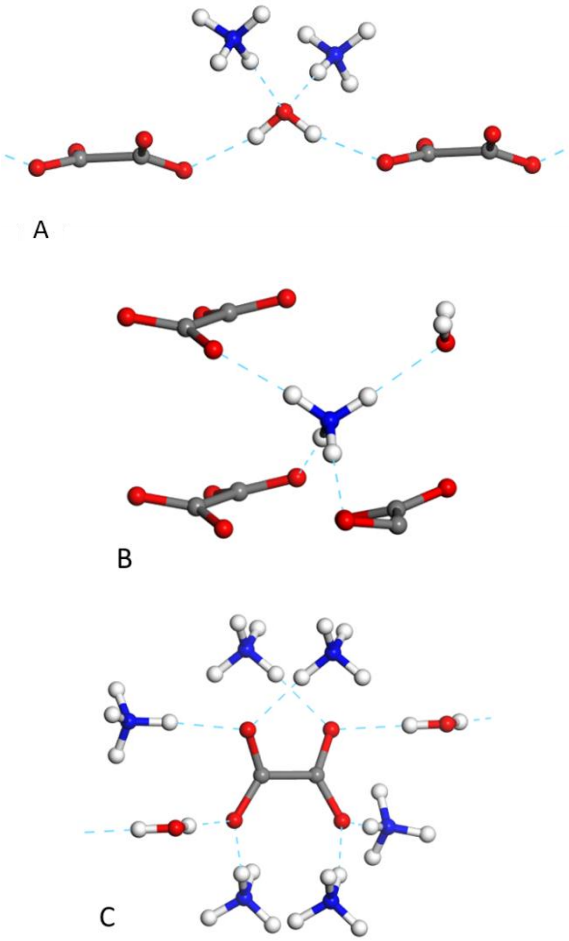

Figure 2. Hydrogen bond structure in oxammite mineral. A, B, and C show the hydrogen bonds surrounding the water molecules, ammonium, and oxalate fragments, respectively. Color code: N= blue, C = gray, O = red, H = white.

The values of the computed bond distances and bond angles are shown in Table 2 and Table 3, respectively, where they are compared with the corresponding experimental values reported by

Taylor and Sabine [46]. The oxammite unit cell only contains one inequivalent N atom, one C atom, two oxalate O atoms, and one water O atom (Ow). The C-C, C-O1, and C-O2 internal oxalate fragment bond distances were calculated as 1.574, 1.264, and 1.248 Å, respectively, which are comparable to the observed values of 1.565, 1.254, and 1.266 Å. Thus, the oxalate anion is described very well (the O1-C-O2, O1-C-C and O2-C-C bond angles are also reproduced satisfactorily, as shown in Table 3). The structure of the ammonium cation as well as the distances and angles in the hydrogen bond network are also described well (see Table 2 and Table 3).

Table 2. Bond distances in the crystal structure of oxammite (in Å).

Distance	Exp. [46]	Calc.
C-C	1.565	1.574
C-O1	1.254	1.264
C-O2	1.248	1.266
N-H2	0.943	1.050
N-H4	0.951	1.049
N-H1	0.966	1.050
N-H3	0.974	1.050
Ow-Hw	0.887	0.994
N-H4…O2	2.835	2.800
N-H5…O1	2.850	2.828
N-H3…Ow	2.905	2.835
N-H2…O2	3.172	3.141
Ow-Hw-O1	2.767	2.721

Table 3. Bond angles in the crystal structure of oxammite (in degrees).

Angle	Exp. [46]	Calc.
O1-C-O2	125.9	125.23
O1-C-C	116.7	117.47
O2-C-C	117.4	117.30
H2-N-H1	111.3	112.00
H2-N-H4	112.7	110.03
H2-N-H3	106.6	109.19
H4-N-H3	109.6	110.03
H3-N-H1	113.5	108.39
H1-N-H4	103.0	107.17
Hw-Ow-Hw	104.0	109.85
N-H1-O2	169.7	172.03
N-H2-Ow	175.2	174.15
N-H3-O2	175.1	178.08
N-H4-O1	172.4	169.29
Ow-Hw-O1	163.4	165.37

3.2. X-Ray powder diffraction pattern

The X-ray powder diffraction pattern for oxammite was derived from the experimental structures determined by Robertson at 30 K [44], by Taylor and Sabine [46] at room temperature, and from the structure calculated using CuK_α radiation (λ = 1.540598 Å) [81]. The most intense lines (I > 10%) are shown in Figure 3, which indicates that the line positions and intensities in both patterns are in very good agreement. The values of the main reflections are given in Table 4. This table demonstrates that the agreement with the results given by Taylor and Sabine [46] is very good, but the agreement with those reported Robertson [44] at 30 K is excellent. The computer code XPowder [89] using the PDF-2 database [90] identified the calculated pattern as that of oxammite (diffractogram 87-660, corresponding to the synthetic oxammite sample given by Taylor and Sabine [46]).

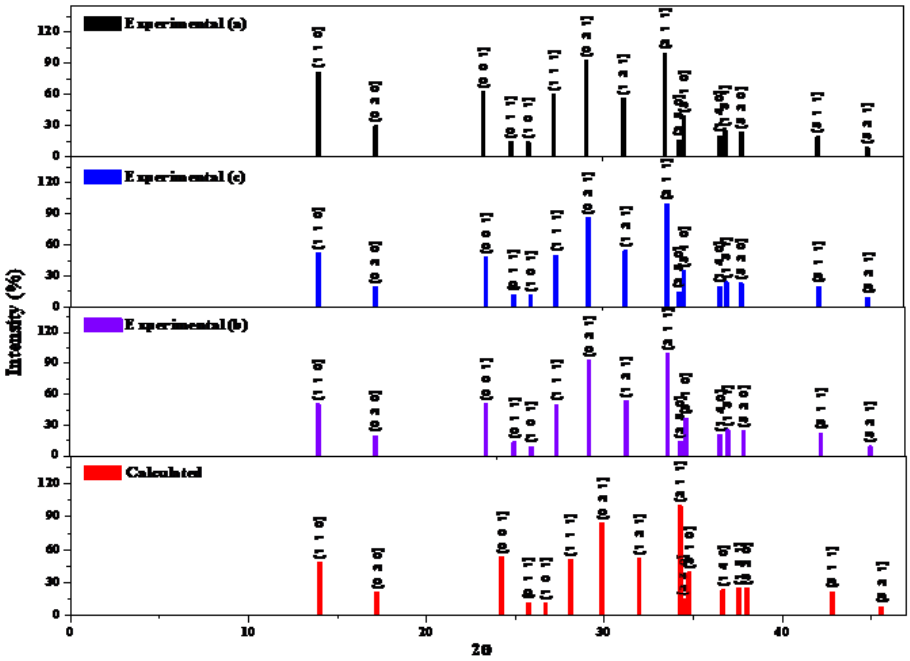

Figure 3. X-ray powder diffraction pattern of oxammite obtained using CuK_α radiation: a) experimental diffractogram (pattern 87-660 from the PDF-2 database); b) X-ray powder pattern computed from the experimental geometry determined by Robertson at 30 K [44]; c) X-ray powder pattern computed from the experimental geometry obtained by Taylor and Sabine at 298.15 K [46]; and d) X-ray powder pattern computed from the calculated geometry.

Table 4. Main reflections in the X-ray powder diffraction pattern for oxammite: a) experimental diffractogram (pattern 87-660 from the PDF-2 database); b) X-ray powder pattern computed from the experimental geometry determined by Robertson at 30 K [44]; c) X-ray powder pattern computed from the experimental geometry obtained by Taylor and Sabine at 298.15 K [46]; and d) X-ray powder diffractogram computed from the calculated geometry.

Experimental (a)				Experimental (b)			Experimental (c)			Calculated (d)		
2Θ	**d (Å)**	**I (%)**	**[hkl]**	**2Θ**	**d (Å)**	**I (%)**	**2Θ**	**d (Å)**	**I (%)**	**2Θ**	**d (Å)**	**I (%)**
13.98	6.329	81.9	[1 1 0]	13.982	6.3286	50.415	13.963	6.3374	52.639	14.017	6.3129	48.704
17.21	5.148	30.3	[0 2 0]	17.189	5.1545	20.045	17.189	5.1545	19.737	17.214	5.1471	21.333
23.29	3.816	62.8	[0 0 1]	23.422	3.7950	50.800	23.422	3.7950	47.872	24.229	3.6704	53.619
24.86	3.578	14.9	[0 1 1]	24.983	3.5614	13.378	24.983	3.5614	12.339	25.748	3.4572	11.963
25.83	3.446	14.3	[1 0 1]	25.955	3.4301	9.1380	25.944	3.4315	11.220	26.705	3.3355	11.608
27.27	3.267	60.0	[1 1 1]	27.381	3.2547	50.100	27.370	3.2559	50.088	28.099	3.1730	51.218
29.10	3.066	92.9	[0 2 1]	29.199	3.0561	92.732	29.199	3.0561	86.638	29.875	2.9884	84.500
31.20	2.864	56.4	[1 2 1]	31.299	2.8556	53.564	31.290	2.8564	54.543	31.947	2.7991	51.813
33.53	2.670	100.0	[2 1 1]	33.636	2.6624	100.00	33.601	2.6650	100.00	34.270	2.6145	100.00
34.35	2.608	16.5	[2 3 0]	34.346	2.6089	14.418	34.312	2.6114	14.858	34.422	2.6033	14.825
34.61	2.589	39.5	[3 1 0]	34.648	2.5868	37.096	34.573	2.5923	34.835	34.756	2.5791	39.957
36.63	2.451	20.4	[1 4 0]	36.595	2.4536	20.737	36.587	2.4541	20.075	36.655	2.4497	23.269
36.93	2.432	25.8	[1 3 1]	37.000	2.4276	25.622	36.992	2.4281	24.536	37.576	2.3917	25.047
37.86	2.374	24.1	[3 2 0]	37.893	2.3724	24.708	37.824	2.3766	23.442	38.002	2.3659	25.473
42.14	2.143	19.6	[3 1 1]	42.247	2.1375	22.560	42.183	2.1406	19.981	42.819	2.1102	21.669
44.93	2.016	9.1	[3 2 1]	45.028	2.0117	9.396	44.968	2.0142	9.327	45.581	1.9886	8.411
49.03	1.856	7.3	[1 0 2]	49.312	1.8465	9.620	49.306	1.8467	8.612	51.019	1.7886	7.466
49.72	1.832	8.4	[2 5 0]	49.686	1.8335	9.265	49.661	1.8343	9.194	49.781	1.8302	8.983
49.88	1.827	10.2	[1 1 2]	50.151	1.8176	9.028	50.144	1.8178	8.688	51.840	1.7622	7.921

3.3. Raman spectrum band assignment

The experimental Raman shifts obtained in the experimental studies by Frost *et al.* [24-26] and Clark and Firth [47] as well as their corresponding empirical assignments are compared in Table 5. Frost *et al.* [24] recorded the Raman spectra for oxammite using a natural sample that originated from Guanape Island in Peru, whereas Clark and Firth [47] used a synthetic material. The Raman spectra provided by Frost *et al.* [24] were obtained using exciting radiation from a Nd-Yag laser (780 nm) at a resolution of 2 cm^{-1}, and those reported by Clark and Firth [47] were recorded by exciting the sample with radiation at 514.5 nm from a Coherent I70 Ar^{+} laser with an estimated accuracy of about 1 cm^{-1}. As shown in Table 5, the band wavenumbers were very similar for both spectra, but the assignments were incomplete and significantly different. Thus, we conducted a rigorous assignment of the bands in the Raman spectra, which was not based on empirical arguments or force field computations.

The Raman spectrum (calculated at T = 298 K, λ = 532 nm, and full width at half-maximum of 5 cm^{-1}) computed in the wavenumber range of 3500–0 cm^{-1} is shown in Figure 4, where the experimental [24-26] and computed spectra are separated into four zones: (A) 3500 to 1800 cm^{-1} (Figure 4A); (B) 1800 to 1200 cm^{-1} (Figure 4B); (C) 1200 to 750 cm^{-1} (Figure 4C); and (D) 750 to 150 cm^{-1} (Figure 4D). It should be noted that the range of the Raman shifts shown in some of these figures is only part of the full region in order to present the bands in the corresponding region in a clear manner. The Raman shifts of these spectra and the computed intensities and assignments are given in Table 6. Graphical representations of the vibrational atomic motions in the most relevant Raman active normal modes are shown in Figure S1 in the Supplementary Information. The results obtained in each spectral zone are discussed separately in the following.

Table 5. Comparison of experimental Raman shifts and assignments.

Exp. Raman shift [24] (cm^{-1})	Exp. Raman shift [47] (cm^{-1})	Assignment [24]	Assignment [47]
3500–1800 cm^{-1} region			
3235	3237	ν^s / $\nu^a(OH)$	$\nu_3(NH_4)$
3030	3028		$\nu_1(NH_4)$
2995	-		-
2900	-	ν^s / $\nu^a(NH)$	-
2879	2878		$2\nu_4(NH_4)$
-	2344	-	$\nu_s(CO_2) + \delta_s(CO_2)$
2161	2167	-	-
-	1933	-	$\nu_s(CO_2) + \nu(CC)$
1902	1895	-	$\nu_s(CO_2) + \rho(CO_2)$
1800–1100 cm^{-1} region			
1737	1744	–	-
-	1726	-	$\nu_2(NH_4)$
1695	1699	$\nu^a(CO)$	-
1605	1601		$\nu_a(CO_2)$
1473	1475		$\nu_4(NH_4)$
1451	1450	$\nu^s(CO) + \nu(CC)$	$\nu_s(CO_2)$
1447	-		-
1430	1428		$\nu_4(NH_4)$
1417	-	$\nu^s(CO) + \delta(OCO)$	-
1312	1313		$\nu_a(CO_2)$
1100–750 cm^{-1} region			
892	894		$\delta_s(CO_2)$
866	868	$\nu^s(CO) + \delta(OCO)$	–
815	-		-
750–150 cm^{-1} region			
642	641	$\delta(OCO) + \nu(MO)$	$\rho_w(CO_2)$
489	491	$Ring\ deform. + \delta(OCO)$	$\nu(CC)$
438	443	$\nu(MO)$ $+$ $Ring\ deform.$	$\rho_r(CO_2)$
278	-	$Out\ of\ plane\ bending$	-
224	228	$Lattice\ modes$	-
210	213		-
198	198		-
181	184		-
160	160		-

(A) 3500 to 1800 cm^{-1} region

The first band observed in this region had a Raman shift of 3235 cm^{-1}. The calculated wavenumber associated with this band was 3183 cm^{-1}. The corresponding vibration had A symmetry (see Table 6). The band could be assigned to symmetric OH bond stretching vibrations, $\nu^s(OH)$. However, Clark and Firth [47] assigned this band to NH bond stretching vibrations (see Table 5). The second experimental band was found at 3030 cm^{-1}. This second band was described

experimentally as a single band, but it was shown theoretically to contain two nearly coincident contributing bands. The corresponding computed values were 3002 and 3001 cm^{-1} , and the corresponding vibrations had B_2 and B_3 symmetries, respectively. This band was ascribed to OH bond stretching vibrations in the experimental studies by Frost *et al.* [24-26], but these bands must be assigned to NH bond stretching vibrations, $\nu(NH)$ (see the vibrational mode images in Figure S1 in the Supplementary Information).

The next bands in the experimental spectrum were found at 2995 and 2900 cm^{-1} where both again corresponded to two contributing bands. The calculated wavenumbers of these bands were 2984 and 2981 cm^{-1} (both having A symmetry) and 2955 and 2936 cm^{-1} (A and B_3 symmetries), respectively. These four bands were assigned to NH bond stretching vibrations. It should be noted that the bands at 2995 and 2900 cm^{-1} were not found by Clark and Firth [47]. The band at 2879 cm^{-1} did not appear in the computed spectrum and it was recognized as an overtone $2\nu_1$ (ν_1 = 1430 cm^{-1}), thereby confirming the assignment of this band by Clark and Firth [47].

It should be noted that due to the distortion of the ammonium fragment symmetry with respect to the tetrahedral symmetry, the NH bond stretching vibrations were not symmetric or antisymmetric. For comparison, the wavenumbers for the three-fold degenerate antisymmetric and non-degenerate symmetric CH bond stretching vibrations of the isolated tetrahedral CH_4 molecule were 3157 and 3025 cm^{-1} [91-92], respectively , and the corresponding values for the NH bond stretching vibrations of the ammonium fragment were approximately 3145 and 3040 cm^{-1} [93]. In addition, in the spectrum for the free ammonium fragment, an overtone was located at about 2800 cm^{-1}, [93], which is comparable to the value of 2879 cm^{-1} for the overtone band found for the oxammite mineral.

Finally, the four bands observed by Frost *et al.* [24-26] and Clark and Firth [47] at 2344, 2161, 1933, and 1902 cm^{-1} did not appear in the computed spectrum. These bands appeared to be combination bands: $\nu_1+\nu_2$ (where ν_1, ν_2 = (1695, 642), (1312, 866), (1447, 489), and (1417, 489) cm^{-1}, respectively). The bands located at 1695, 1447, 1417, 1312, 866, 642, and 489 cm^{-1} are described in the following.

(B) 1800 to 1200 cm^{-1} region

In this zone, we first observed four weak experimental bands at wavenumbers of 1737, 1726, 1695, and 1605 cm^{-1} corresponding to the theoretical bands located at 1745, 1725, 1697, and 1554 cm^{-1} , respectively (B_3, A, B_1 , and B_1 symmetries). The first three bands were assigned to HNH bending vibrations and the fourth to HOH bending vibrations. The band at 1726 cm^{-1} was not found in the experimental studies by Frost *et al.* [24-26]. The bands at 1737 and 1695 cm^{-1} were not assigned by Frost *et al.* [24-26] or Clark and Firth [47]. Furthermore, the last band was assigned to CO bond stretching vibrations in these previous studies. The wavenumber of the two-fold degenerate HCH bending vibration in the free CH_4 molecule was 1583 cm^{-1}, [91-92] and the corresponding HNH bending vibration for the free ammonium fragment was located at approximately 1680 cm^{-1} [93].

The next experimental bands were found at 1473, 1451, and 1447 cm^{-1} and the associated calculated Raman shifts were 1484, 1473, 1459, and 1429 cm^{-1} , respectively (the first of the observed bands corresponded to two calculated bands, and the associated symmetries were A_1, B_2, B_2 , and B_3,). The band at 1447 cm^{-1} was not found by Clark and Firth [47]. Frost *et al.* [24-26] assigned these bands to a combination of the stretching vibrations of CO and CC bonds, $\nu^s(CO)+\nu(CC)$, but they should be assigned to ammonium $\varrho(NH_4)$ deformation vibrations (out of plane bending vibrations) according to the vibrational mode images shown in Figure S1 in the

Supplementary Information. The corresponding wavenumber for the three-fold degenerate $\nu_4(CH_4)$ vibration in the free CH_4 molecule was 1367 cm^{-1} [91-92] and that for the free ammonium fragment $\nu_4(NH_4)$ was at approximately 1400 cm^{-1} [93]. Again, it should be noted that the ammonium fragment symmetry was lost in the oxammite mineral, and thus the symbol ϱ, was used instead of ν_4,. Clark and Firth [47] also assigned the band at 1473 cm^{-1} to ammonium fragment deformations but they attributed the band at 1451 cm^{-1} to the stretching vibrations of CO bonds.

The last three experimental bands in this region of the Raman spectrum were found at 1430, 1417, and 1312 cm^{-1}, and they were reproduced theoretically at 1391, 1390, and 1277 cm^{-1} , respectively (symmetries of A, B_1 and B_3). The first two bands were assigned to a combination of the stretching vibrations of CO and CC bonds, $\nu^s(CO)$+ $\nu(CC)$, and the last must be assigned to a combination of CO bond stretching vibrations and CC bond translations, $\nu^s(CO)$+ $T(CC)$. The first band received the same assignment in the experimental studies by Frost *et al.* [24-26], but the other two were attributed to combinations of CO bond stretching vibrations and OCO bending vibrations. Clark and Firth [47] did not assign the second band, but attributed the first and third bands to ammonium deformations and CO bond stretching vibrations, respectively.

(C) 1200 to 750 cm^{-1} region

The two most important experimental bands within this spectral region had Raman shifts of 892 and 866 cm^{-1} , and the corresponding calculated bands had wavenumbers of 848 and 837 cm^{-1}, respectively. The vibrations associated with these bands had A and B_2 symmetries. The first of these bands must be assigned to HOH twisting vibrations, $t(HOH)$, and the second to oxalate anion deformation vibrations, $\varrho(C_2O_4)$. The last band was analogous to that found in natroxalate mineral [49] at 875 cm^{-1}, and the atomic motion in the associated vibration involved a CC bond

rotation (see the vibrational mode image in Figure S1 in the Supplementary Information). These two assignments differ from those given by Frost *et al.* [24-26] and Clark and Firth [47]. A third very weak band was also reported by Frost *et al*. [24-26] at 815 cm^{-1}. This band was not found by Clark and Firth [47] and it was absent from the theoretical spectrum. It is possible that this band was the result of a combination of two bands, $\nu_1+\nu_2$ (ν_1, ν_2 = 642, 181 cm^{-1}).

Table 6. Experimental and calculated Raman band wavenumbers, calculated intensities, and assignments.

Exp. Raman shift (cm^{-1})	Calc. Raman shift (cm^{-1})	Irr. Rep. (C_{2h})	Int. (Å^4)	Assignment (this study)
3500–1800 cm^{-1} region				
3235[a], 3237[b]	3183	A	1502.3	$\nu^s(OH)$
3030[a], 3028[b]	3002	B_2	666.7	$\nu(NH)$
	3001	B_3	400.3	$''$
2995[a]	2984	A	812.5	$''$
	2981	A	866.4	$''$
2900[a]	2955	A	2211.3	$''$
	2936	B_3	1008.6	$''$
2879[a], 2878[b]	-	-		$2\nu_1$ ($\nu_1 = 1430\ cm^{-1}$)
2344[b]	-	-	-	$\nu_1+\nu_2$ ($\nu_1 = 1695\ cm^{-1}$; $\nu_2 = 642\ cm^{-1}$)
2161[a], 2167[b]	-	-	-	$\nu_1+\nu_2$ ($\nu_1 = 1312\ cm^{-1}$; $\nu_2 = 866\ cm^{-1}$)
1933[b]	-	-	-	$\nu_1+\nu_2$ ($\nu_1 = 1447\ cm^{-1}$; $\nu_2 = 489\ cm^{-1}$)
1902[a], 1895[b]	-	-	-	$\nu_1+\nu_2$ ($\nu_1 = 1417\ cm^{-1}$; $\nu_2 = 489\ cm^{-1}$)
1800–1100 cm^{-1} region				
1737[a], 1744[b]	1745	B_3	4.7	$\delta(HNH)$
1726[b]	1725	A	9.8	$''$
1695[a], 1697[b]	1697	B_1	23.6	$''$
1605[a], 1601[b]	1554	B_1	25.0	$\delta(HOH)$
1473[a], 1475[b]	1484	A	26.1	$\varrho(NH_4)$
	1473	B_2	7.9	$''$
1451[a], 1450[b]	1459	B_2	4.8	$''$
1447[a]	1429	B_3	23.0	$''$
1430[a], 1428[b]	1391	A	218.7	$\nu^s(CO)+\nu(CC)$
1417[a]	1390	B_1	12.3	
1312[a], 1313[b]	1277	B_3	15.6	$\nu^s(CO)+T(CC)$
1100–750 cm^{-1} region				
892[a], 894[b]	848	A	38.7	$t(HOH)$
866[a], 868[b]	837	B_2	2.3	$\varrho(C_2O_4)$
815[a]	-	-	-	$\nu_1+\nu_2$ ($\nu_1 = 642\ cm^{-1}$; $\nu_2 = 181\ cm^{-1}$)
750–150 cm^{-1} region				
642[a], 641[b]	622	B_1	2.4	$\varrho(C_2O_4) + \rho(HNH)$
489[a], 491[b]	481	B_1	6.2	$\delta(OCO) + \nu(CC) + \rho(HNH)$
	462	A	17.7	$\delta(OCO) + \nu(CC) + t(HNH)$
438[a], 443[b]	431	B_1	3.9	$\varrho(C_2O_4) + t(HNH)$
278[a]	277	B_2	2.3	$T(NH_4)$
224[a], 228[b]	262	B_3	7.5	$T(H_2O) + T(NH_4)$
	254	B_1	2.6	$T(H_2O) + T(NH_4)$
210[a], 213[b]	225	A	4.0	$T(NH_4)$
198[a], 198[b]	186	B_2	1.2	$T(C_2O_4) + T(H_2O) + T(NH_4)$
181[a], 184[b]	172	B_1	1.1	$T(H_2O) + T(NH_4)$
160[a], 160[b]	158	A	0.5	$T(H_2O) + T(NH_4)$

[a] From Frost *et al*. [24-26]; [b] From Clark and Firth [47].

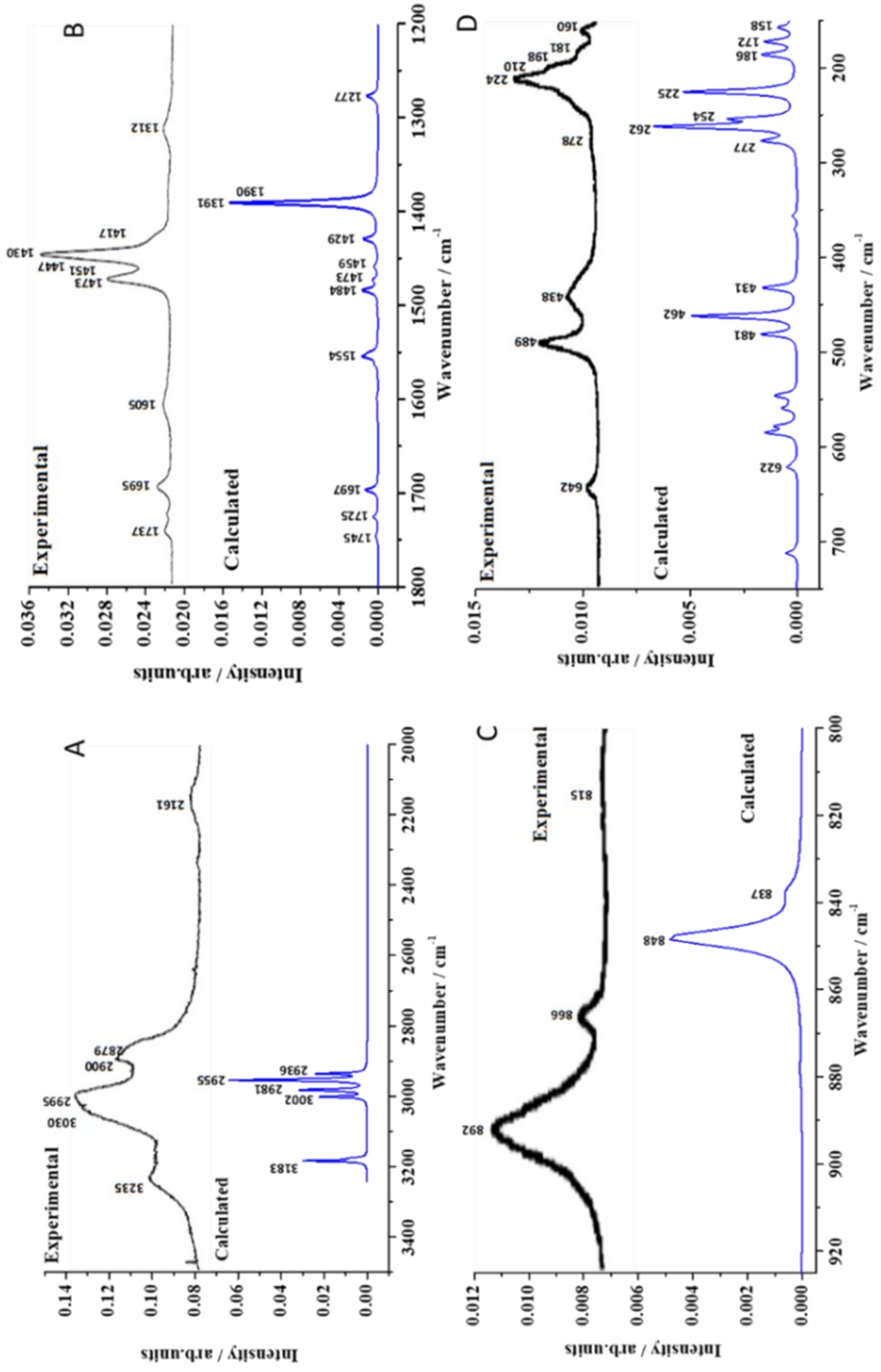

Figure 4. Experimental [24-26] and theoretical Raman spectra obtained for oxammite mineral. (A) region: 3500–2000 cm^{-1}; (B) region: 1800–1200 cm^{-1}; (C) region: 1200–750 cm^{-1}; and (D) region: 750–150 cm^{-1}.

(D) 750 to 150 cm^{-1} region

The first band in this region of the experimental spectrum was located at 642 cm^{-1} and it was reproduced theoretically at 622 cm^{-1}. The corresponding vibration had B_1 symmetry and it was attributed to a combination of oxalate fragment deformations and HNH rocking vibrations. The next band was observed at 489 cm^{-1} and theoretical computations showed that it contained two contributing bands. The corresponding computed values were 481 and 462 cm^{-1} and the corresponding vibrations had B_1 and A symmetries, respectively. These bands must be ascribed to combinations of OCO bending, CC bond stretching, and HNH rocking and twisting vibrations. The experimental bands at 438 and 278 cm^{-1} were reproduced very well theoretically at 431 and 277 cm^{-1} , respectively (B_1 and B_2 symmetries). The first of these bands was assigned to oxalate fragment deformations plus HNH twisting vibrations and the second to ammonium fragment translations.

The band observed at 224 cm^{-1} corresponded to the pair of computed bands located at 262 and 254 cm^{-1} (B_3 and B_1 symmetries), which were both attributed to ammonium and water translations. Finally, the bands observed at 210, 198, 181, and 160 cm^{-1} were calculated at 225, 186, 172, and 158 cm^{-1} , respectively (A, B_2, B_1 , and A symmetries). All of these bands were assigned to unspecified lattice modes in previous experimental studies [24-26], but the theoretical calculations allowed the corresponding translational motions associated with these vibrations to be fully assigned, as shown in Table 6.

3.4. Thermodynamic properties

3.4.a. Heat capacities, entropies, enthalpies, and Gibbs free energies

The isobaric heat capacity, entropy, enthalpy, and free energy functions computed for the oxammite mineral phase are shown in Figures 5A, 5B, 5C, and 5D, respectively. All of the enthalpy and free energy values were divided by the temperature in order to use the same units for these properties as the heat capacity and entropy ($J \cdot K^{-1} \cdot mol^{-1}$). The detailed values of the computed thermodynamic functions over the temperature range from 0 to 1000 K are given in Table S1 to S4 in the Supplementary Information, and a subset of values for the calculated thermodynamic functions over the temperature range from 298.15 to 900 K is shown in Table 7.

Table 8 shows the values computed for the specific heat of ammonium oxalate at 323 and 298.15 K, which are compared with the specific heat measurements given by Satoh and Sogabe [94-95] and Cox *et al*. [96-97]. The calculated and experimental values at 323 K were in good agreement, where the difference was about 4%. It should be noted that the experimental value reported at 298.15 K [96-97] was obtained for anhydrous ammonium oxalate, and thus this value may serve as a reference but it is not rigorously comparable with our calculated value. The computed value of the heat capacity at the highest temperature considered (1000 K), 358.65 $J \cdot K^{-1} \cdot mol^{-1}$, was 24.3% lower than the Dulong–Petit asymptotic limit of 473.91 $J \cdot K^{-1} \cdot mol^{-1}$,.

As mentioned in the Methods section, the thermodynamic functions were also calculated for the oxammite mineral phase but without applying symmetry restrictions and using an extended k-mesh comprising 21 k points. The specific heat obtained at 323 K was 204.01 $J \cdot K^{-1} \cdot mol^{-1}$, which differed by only 0.8% from the calculated value given in Table 8.

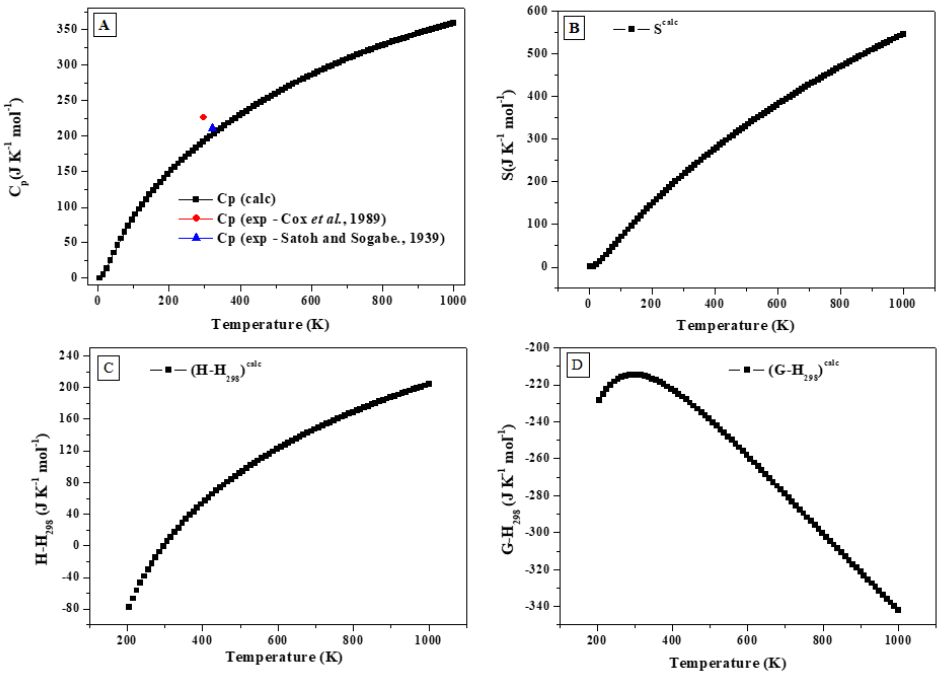

Figure 5. Calculated thermodynamic properties of oxammite mineral: A) isobaric specific heat; B) entropy; C) enthalpy; and D) Gibbs free energy. All of the properties are given as functions of temperature.

Table 7. Isobaric heat capacity, entropy, enthalpy, and free energy functions calculated for oxammite mineral. All of the values are given in units of $J \cdot K^{-1} \cdot mol^{-1}$.

T(K)	C_p^{calc}	S^{calc}	$(H-H_{298})^{calc}$	$(G-H_{298})^{calc}$
298.15	192.7051	214.6138	0.0	–214.6596
360	215.8214	253.0950	35.1634	–217.9313
380	222.7515	264.9508	44.8587	–220.0913
400	229.4486	276.5476	53.9145	–222.6319
420	235.9277	287.8999	62.4151	–225.4835
440	242.2010	299.0205	70.4305	–228.5889
460	248.2788	309.9212	78.0189	–231.9016
480	254.1696	320.6126	85.2285	–235.3839
500	259.8808	331.1044	92.0988	–239.0059
520	265.4186	341.4054	98.6626	–242.7437
540	270.7885	351.5236	104.9466	–246.5782
560	275.9958	361.4662	110.9735	–250.4941
580	281.0452	371.2400	116.7623	–254.4791
600	285.9414	380.8511	122.3295	–258.5228
620	290.6892	390.3052	127.6900	–262.6160
640	295.2934	399.6076	132.8571	–266.7507
650	297.5432	404.2035	135.3722	-268.8312
700	308.2946	426.6528	147.3244	-279.3270
800	327.5650	469.1074	168.6686	-300.4389
900	344.2294	508.6758	187.2357	-321.4390

Table 8. Comparison of the calculated and experimental heat capacities for oxammite mineral. All of the values are given in units of $J \cdot K^{-1} \cdot mol^{-1}$. It should be noted that the experimental value for the temperature of 298.15 K was obtained for anhydrous ammonium oxalate [96-97].

T (K)	Exp.	Calc.	Difference (%)
323	211.7[a]	202.3242	–4.4
298.15	226.0[b]	192.7051	–14.7

[a] Satoh and Sogabe [94-95]; [b] Cox *et al.* [96-97].

3.4.b. Enthalpies and Gibbs free energies of formation

The thermodynamic functions of oxammite (given in Section 3.4.a) were used to obtain the enthalpies and free energies of formation for this mineral phase in terms of the elements as a function of temperature. The methods employed were described previously [70] and they produced very accurate results, even for the complex uranyl mineral phases such as metaschoepite at high temperatures [69-70]. Based on the experimental values of the thermodynamic functions for N, C, O, and H atoms given in the JANAF (Joint Army-Navy-Air Force) tables [98], the thermodynamic functions computed for oxammite, and the value of the standard enthalpy of formation reported by Wagman *et al.* [97], $\Delta_f H^0 = -1425.5\ kJ/mol$, we obtained the thermodynamic properties of formation for oxammite as a function of temperature, as presented in Table 9. The results are also shown in Figure 6.

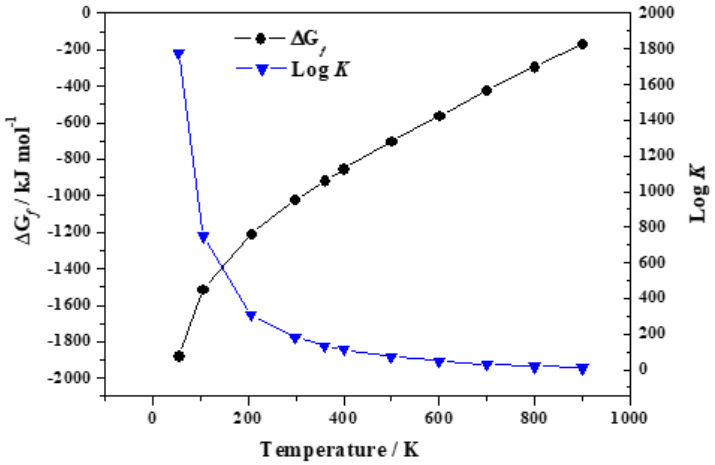

Figure 6. Calculated free energies of formation and reaction constants for oxammite as a function of temperature.

Table 9. Enthalpies ($\Delta_f H$), free energies ($\Delta_f G$) of formation, and reaction constants (Log K) calculated for oxammite as functions of temperature. The values of $\Delta_f H$ and $\Delta_f G$ are in units of kJ/mol.

T(K)	$\Delta_f H$	$\Delta_f G$	Log *K*
55.2525	–1932.1539	–1880.0242	1777.2923
105.5051	–1639.4804	–1512.1678	748.6422
206.0101	–1476.4618	–1207.9315	306.2678
298.15	–1425.5000	–1024.0848	179.4108
360	–1408.6643	–917.7377	133.1569
400	–1401.9631	–853.1634	111.4089
500	–1394.5731	–701.5166	73.2851
600	–1396.0100	–559.5627	48.7130
700	–1403.4735	–424.6621	31.6879
800	–1415.2953	–295.1996	19.2741
900	–1430.7166	–170.3897	9.8889

3.4.c. Thermal decomposition temperature of oxammite

Ammonium oxalate monohydrate is used frequently as a starting material in the laboratory. For instance, it may be employed in the production of hydrogen cyanide [42]. Therefore, as shown for many other oxalate materials, investigating its thermal decomposition may be advantageous in terms of cost and time management during industrial production. As an application of the computed thermodynamic functions of formation, as reported in Section 3.4.b, the thermodynamic properties can be determined easily for the thermal decomposition of oxammite into ammonia, water, carbon monoxide, and carbon dioxide. This reaction may be written as follows [99-102].

$$(NH_4)_2(C_2O_4) \cdot H_2O\ (cr) \rightarrow \quad 2\ NH_3(g) + \ \ 2\ H_2O\ \ (l) + CO\ (g) + CO_2\ (g) \qquad (1)$$

By employing the relationships reported in a previous study [71] and using the experimental thermodynamic functions given for ammonia, water, carbon monoxide, and carbon dioxide by Chase *et al.* [98], as well as the thermodynamic functions calculated for the formation of oxammite (Section 3.4.b), we obtained the enthalpies, free energies, and associated reaction constants for this reaction as a function of temperature, as shown in Table 10. The results are also shown in Figure

7. The calculations showed that the free energy for the reaction becomes negative at a temperature of 288 K (15°C), and, thus ammonium oxalate monohydrate begins to decompose at low temperatures [99-101].

Table 10. Calculated enthalpies ($\Delta_r H$), free-energies ($\Delta_r G$) and associated reaction constants (Log K) of the reaction of thermal decomposition of oxammite as a function of temperature. The values of $\Delta_r H$ and $\Delta_r G$ are in units of kJ/mol.

T(K)	$\Delta_r H$	$\Delta_r G$	Log K
280	211.3538	10.8491	–2.0239
298.15	200.9638	–14.3863	2.5203
320	189.6560	–43.5703	7.1119
340	180.3232	–69.2645	10.6409
360	171.6404	–94.3082	13.6834
380	164.1029	–118.2093	16.2486
400	157.0296	–141.6545	18.4977
420	150.5444	-164.5213	20.4607
440	144.5932	–186.8718	22.1839
460	139.1352	-208.7538	23.7041
480	134.1401	–230.2108	25.0514
500	129.5949	–251.2741	26.2498

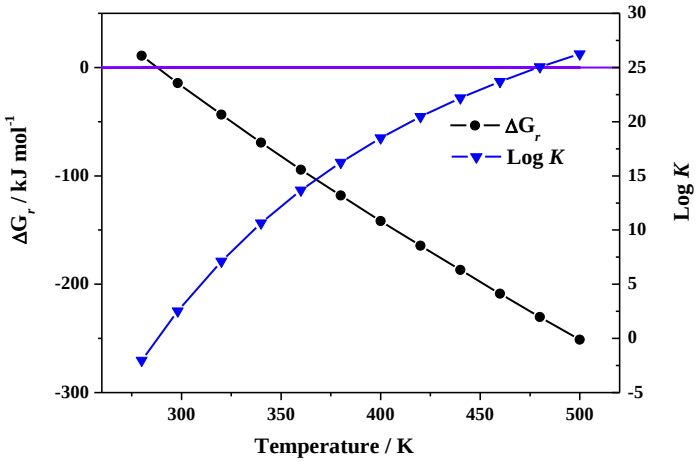

Figure 7. Calculated free energies and reaction constants for the thermal decomposition reaction of oxammite mineral as functions of temperature.

4. Conclusions

In this study, the structural properties, main characteristics of the Raman spectrum, and thermodynamic properties of the ammonium oxalate monohydrate mineral oxammite, $(NH_4)_2(C_2O_4)\cdot H_2O$, were investigated in theoretical solid-state calculations based on the periodic DFT using plane waves and pseudopotentials. The calculated structural properties comprising the lattice parameters, bond lengths and angles, and X-ray powder diffraction patterns were in excellent agreement with the experimental results obtained from low temperature X-ray diffraction data.

The Raman spectrum was also computed at the optimized geometry. The computations were also conducted with a larger k mesh and by relaxing the symmetry constraints and produced essentially the same results. The unscaled wavenumbers were in good agreement with the experimental data, and thus normal mode analysis was performed to assign the most important bands in the observed Raman spectrum. All of the observed bands were assigned to specific vibrational motions, including those at very low wavenumbers. The previous assignments of the Raman spectra were incomplete and based on empirical arguments [24-26,47]. The theoretical calculations allowed us to assign the bands at 2344, 2161, 1933, 1902, 1745, and 1725 cm^{-1}, which were not assigned in previous experimental studies. The bands at 2344, 2161, 1933, and 1902 cm^{-1}, which were absent from the computed spectrum, were identified as combination bands (this also applied to the 815 cm^{-1} band). The band at 2879 cm^{-1} was confirmed as an overtone [47]. Many of the observed bands that were assigned empirically in previous studies were re-assigned. Furthermore, many of the observed bands, such as those located at 3030, 2995, 2900, 1475, 489, and 224 cm^{-1}, were shown to have two contributing bands. All of these uncommon

features were also found in our previous study of the sodium oxalate mineral natroxalate [49], and thus they are likely to occur in the spectra of other oxalate minerals [24-26].

The main bands in the stretching region were those associated with the Raman shifts at 3235, 3030, 2995, and 2900 cm^{-1}, which were reproduced theoretically at 3183, 3002, 2981, and 2955 cm^{-1}, respectively. The first band was assigned to the symmetric OH bond stretching vibration and the others to NH bond stretching vibrations. However, the band at 3030 cm^{-1} was previously assigned to OH stretching vibrations, whereas we showed that it had two contributing bands (the corresponding computed wavenumbers were 3002 and 3001 cm^{-1}).

The most important bands used to fingerprint this mineral are those located at 1430, 892, 489 and 224 cm^{-1} which were reproduced theoretically at 1391, 848, 462, and 262 cm^{-1}., respectively, and these bands were assigned to a combination of CO and CC bond stretching vibrations; HNH twisting vibrations; a combination of OCO bending, CC stretching, and HNH twisting vibrations; and ammonium and water translations.

The thermodynamic functions of the oxammite mineral phase comprising the specific heats, entropies, enthalpies, and Gibbs free energies were theoretically determined as functions of temperature. The specific heat calculated at 323 K, $C_p = 202.3\, J \cdot K^{-1} \cdot mol^{-1}$, was in very good agreement with the experimental value, where the difference between the computed and observed values was about 4% [94-95]. The enthalpies and free energies of formation were also obtained for oxammite in terms of the elements and the thermodynamic properties of its thermal decomposition reaction. The results showed that the ammonium oxalate monohydrate crystalline material starts to decompose at a low temperature of 288 K.

Acknowledgement

The calculations were performed with supercomputers at the CTI-CSIC and CESGA centers. I want to thank Dr Ana María Fernández, Dr Laura Bonales, Dr Vicente Timón, and Prof. Victor J. Herrero for reading the manuscript and providing many helpful comments.

Supplementary Information

The Supplementary Information associated with this article contains: 1) Figure S1: images of the atomic motions in the Raman active vibrational modes of oxammite mineral; 2) Tables S1 to S4: heat capacity, entropy, enthalpy, and free energy functions calculated for oxammite mineral.

References

[1] E. Baran, Review: Natural oxalates and their analogous synthetic complexes, J. Coord. Chem. 67 (2014) 3734–3768.

[2] B. A. Hofmann, S. M. Bernasconi, Review of occurrences and carbon isotope geochemistry of oxalate minerals: implications for the origin and fate of oxalate in diagenetic and hydrothermal fluids, Chem. Geol. 149 (1998) 127–146.

[3] T. Echigo, M. Kimata, Crystal chemistry and genesis of organic minerals: a review of oxalate and polycyclic aromatic hydrocarbon minerals, Can. Mineral. 48 (2010) 1329−1358.

[4] Z. Y. Cheng, D. C. Fernández-Remolar, M. R. M. Izawa, D. M. Applin, M. Chong Díaz, M. T. Fernández-Sampedro, M. García-Villadangos, T. Huang, L. Xiao, and V. Parro, Oxalate formation under the hyperarid conditions of the Atacama Desert as a mineral marker to provide clues to the source of organic carbon on Mars, J. Geophys. Res. Biogeosci. 121 (2016) 1593−1604.

[5] J. A. Wesson, M. D. Ward, Pathological biomineralization of kidney stones, Elements 3 (2007) 415−421.

[6] R. Selvaraju, A. Raja, G. Thiruppathi, FT-Raman spectral analysis of human urinary stones, Spectrochim. Acta A 99 (2012) 205–210.

[7] J. P. Pestaner, F. G. Mullick, F. B. Johnson, Calcium oxalate crystals in human pathology: molecular analysis with the laser Raman microprobe, Arch. Pathol. Lab. Medicin. 120 (l996) 537−540.

[8] H. J. Arnott, M. A. Webb, The structure and formation of calcium oxalate crystal deposits on the hyphae of a wood rot fungus, Scan. Electron Microsc. 4 (1983) 1747−1758.

[9] J. E. Chisholm, G. C. Jones, O. W. Purvis, Hydrated copper oxalate, moolooite, in lichens, Mineral. Mag. 51 (1987) 715−718.

[10] A. Frey-Wyssling, Crystallography of the two hydrates of crystalline calcium oxalate in plants, Am. J. Bot. 68 (1981) 130−141.

[11] H. G. M. Edwards, N. C. Russell, M. R. D. Seward, Calcium oxalate in lichen biodeterioration studied using FT-Raman spectroscopy, Spectrochim. Acta A 53 (1997) 99−105.

[12] H. G. M. Edwards, N. C. Russell, M. R. D. Seaward, D. Slarke, Lichen biodeterioration under different microclimates: an FT Raman spectroscopic study, Spectrochim. Acta A 51 (1995) 2091−2100.

[13] G. M. Gadd, Heterotrophic solubilization of metal-bearing minerals by fungi, Mineral. Soc. Ser. 9 (2000) 57−75.

[14] G. M. Gadd, Fungal production of citric and oxalic acid: importance in metal speciation, physiology and biogeochemical processes, Adv. Microb. Physiol. 41 (1999) 47−92.

[15] C. Plassard, P. Fransson, Regulation of low-molecular weight organic acid production in fungi, Fungal Biol. Rev. 23 (1989) 30−39.

[16] S. Weiner, P. M. Dove, An overview of biomineralization processes and the problem of the vital effect, Rev. Mineral. Geochem. 54 (2003) 1−29.

[17] S. Moore, M. J. Beazley, M. R. McCallum, J. Russ, Can calcium oxalate residues from lichen activity reflect past climate change? Preprints of Extended Abstracts presented at the ACS National Meeting, American Chemical Society, Division of Environmental Chemistry 40 (2000) 4−5.

[18] D. M. Applin, M. R. M. Izawa, E. A. Cloutis, D. Goltz, J. R. Johnson, Oxalate minerals on Mars? Earth Planet. Sci. Lett. 420 (2015) 127–139.

[19] D. M. Applin, M. R. M. Izawa, E. A. Cloutis, Reflectance spectroscopy of oxalate minerals and relevance to Solar System carbon inventories, Icarus 278 (2016) 7–30.

[20] J. F. Mustard, M. Adler, A. Allwood, D. S. Bass, D. W. Beaty, J. F. Bell, W. B. Brinckerhoff, M. Carr, D. J. Des Marais, B. Drake, *et al*., Report of the Mars 2020 Science Definition Team, Mars Exploration Program Analysis Group (MEPAG), 2013, 154 pp.

[21] R. C. Wiens, S. Maurice, F. Rull, The SuperCam remote sensing instrument suite for the Mars 2020 Rover: A preview, Spectroscopy 32 (2017) 50–55.

[22] H. G. M. Edwards, I. B. Hutchinson, R. Ingley, N. R. Waltham, S. Beardsley, S. Dowson, S. Woodward, The search for signatures of early life on Mars: Raman spectroscopy and the Exomars mission, Spectrosc. Eur. 23 (2011) 6−15.

[23] F. Rull, J. Martinez-Frias, Raman spectroscopy goes to Mars, Spectrosc. Eur. 18 (2006) 18−21.

[24] R. L. Frost, Y. Jing, Z. Ding, Raman and FTIR spectroscopy of natural oxalates: Implications for the evidence of life on Mars, Chin. Sci. Bull. 48 (2003) 1844−1852.

[25] R. L. Frost, A. Locke, W. N. Martens, Raman spectroscopy of natural oxalates at 298 and 77 K, J. Raman Spectrosc. 34 (2003) 776−785.

[26] R. L. Frost, Raman spectroscopy of natural oxalates, Anal. Chim. Acta 517 (2004) 207−214.

[27] R. L. Frost, A. J. Locke, W. N. Martens, Synthesis and Raman spectroscopic characterisation of the oxalate mineral wheatleyite $Na_2Cu^{2+}(C_2O_4)\cdot 2H_2O$, J. Raman Spectrosc. 39 (2008) 901−908.

[28] R. L. Frost, M. L. Weier, Thermal treatment of weddellite – a Raman and infrared emission spectroscopic study, Thermochim. Acta 406 (2003) 221−232.

[29] J. Jehlicka, H. G. M. Edwards, A. Culka, Using portable Raman spectrometers for the identification of organic compounds at low temperatures and high altitudes: exobiological applications, Phil. Trans. R. Soc. A 368 (2010) 3109–3125.

[30] A. Culka, Application of Raman spectroscopy for study of nitrogen containing compounds for astrobiological purposes, Ph.D. thesis, Charles University, Prague 2011.

[31] B. Salvadori, V. Errico, M. Mauro, L. Dei, Evaluation of gypsum and calcium oxalates in deteriorated mural paintings by quantitative FTIR spectroscopy, Spectrosc. Lett. 36 (2003) 501−513.

[32] I. Lamprecht, A. Reller, R. Riesen, H. G. Wiedemann, Ca-oxalate films and microbiological investigations of the influence of ancient pigments on the growth of lichens, J. Thermal Anal. 49 (1997) 1601−1607.

[33] M. Del Monte, C. Sabbioni, Weddellite on limestone in the Venice [Italy] environment, Environ. Sci. Technol. 17 (l983) 518−522.

[34] H. G. M. Edwards, K. A. E. Edwards, D. W. Farwell, I. R. Lewis, M. R. D. Seaward, An approach to stone and fresco lichen biodeterioration through Fourier transform Raman microscopic investigation of thallus – substratum encrustation, J. Raman Spectrosc. 25 (1994) 99−103.

[35] J. Girbal, J. L. Prada, R. Rocabayera, M. Argemi, Dating of biodeposits of oxalates at the Arc de Bera in Tarragona, Spain, Radiocarbon 43 (2001) 637−645.

[36] L. Maiore, M. C. Aragoni, G. Carcangiu, O. Cocco, F. Isaia, V. P. Meloni, A. Murru, E. Tuveri, M. Arca, Synthesis, characterization and DFT-modeling of novel agents for the protection and restoration of historical calcareous stone substrates, J. Colloid Interface Sci. 448 (2015) 320–330.

[37] P. H. Chang, Y. H. Huang, C. L. Hsueh, M. C. Lu, G. H. Huang, Treatment of non-biodegradable wastewater by electro-Fenton method, Water Sci. Technol. 49 (2004) 213−218.

[38] A. Abd El-Raady, T. Nakajima, P. Kimchhayarasy, Catalytic ozonation of citric acid by metallic ions in aqueous solution, Ozone Sci. Eng. 27 (2005) 495−498.

[39] J. A. Zazo, J. A. Casas, A. F. Mohedano, M. A. Gilarranz, J. J. Rodriguez, Chemical pathway and kinetics of phenol oxidation by Fenton's reagent, Environ. Sci. Technol. 39 (2005) 9295−9302.

[40] W. C. Chu, C. Y. Kwan, K. H. Chan, S. K. Kam, A study of kinetic modelling and reaction pathway of 2,4-dichlorophenol transformation by photo Fenton-like oxidation, J. Hazard. Mater. 121 (2005) 119−126.

[41] C.-H. Liu, Y.-H. Huang, H.-T. Chen, Study of oxalate mineralization using electrochemical oxidation technology, Environ. Eng. Manage. 17 (2007) 345−349.

[42] W. L. Fierce, W. J. Sandner, Method of preparing hydrogen cyanide from oxamide and ammonium oxalate, United States Patents US2942946A (1958).

[43] S. B. Hendricks, M. E. Jefferson, Electron distribution in $(NH_4)_2C_2O_4$–H_2O and the structure of the oxalate group, J. Chem. Phys. 4 (1936) 102–107.

[44] J. H. Robertson, Ammonium oxalate monohydrate: structure refinement at 30K, Acta Cryst. 18 (1965) 410–417.

[45] J. H. Robertson, Enantiomorphism of the oxalate ion in ammonium oxalate monohydrate, Acta Cryst. 18 (1965) 417–419.

[46] J. C. Taylor, T. M. Sabine, Isotope and bonding effects in ammonium oxalate monohydrate determined by the combined use of neutron and X-ray diffraction analyses, Acta Cryst. B 28 (1972) 3340−3351.

[47] R. J. H. Clark, S. Firth, Raman, infrared and force field studies of $K_2{}^{12}C_2O_4{\cdot}H_2O$ and $K_2{}^{13}C_2O_4{\cdot}H_2O$ in the solid state and in aqueous solution, and of $(NH_4)_2\ {}^{12}C_2O_4{\cdot}H2O$ and $(NH_4)_2\ {}^{13}C_2O_4{\cdot}H_2O$, Spectrochim. Acta A 58 (2002) 1731–1746.

[48] M. Cadene, A. Fournel, Phonons optiques de l'oxalate d'ammonium hydraté à 295 et 10 K, J. Mol. Struct. 37 (1977) 35−57.

[49] F. Colmenero, V. Timon, Study of the structural, vibrational and thermodynamic properties of natroxalate mineral using density functional theory, J. Solid State Chem. 263 (2018) 131–140.

[50] Y. Qiao, K. Wang, H. Yuan, K. Yang, B. Zou, Negative linear compressibility in organic mineral ammonium oxalate monohydrate with hydrogen bonding wine-rack motifs, J. Phys. Chem. Lett. 6 (2015) 2755−2760.

[51] R. H. Baughman, S. Stafström, C. Cui, S. O. Dantas, Materials with negative compressibilities in one or more dimensions, Science 279 (1998) 1522−1524.

[52] A. B. Cairns, A. L. Goodwin, Negative linear compressibility, Phys. Chem. Chem. Phys. 17 (2015) 20449−20465.

[53] K. E. Evans, A. Alderson, Auxetic materials: functional materials and structures from lateral thinking! Adv. Mater. 12 (2000) 617−628.

[54] A. E. Aliev, J. Oh, M. E. Kozlov, A. A. Kuznetsov, S. Fang, A. F. Fonseca, R. Ovalle, M. D. Lima, M. H. Haque, Y. N. Gartstein, *et al.*, Giant-stroke, superelastic carbon nanotube aerogel muscles, Science 323 (2009) 1575−1578.

[55] G. M. Spinks, G. G. Wallace, L. S. Fifield, L. R. Dalton, A. Mazzoldi, D. De Rossi, I. I. Khayrullin, R. H. Baughman, Pneumatic carbon nanotube actuators, Adv. Mater. 14 (2002) 1728−1732.

[56] H. Kuppers, Elastic properties of ammonium oxalate hydrate, ammonium hydrogen oxalate hemihydrate, and ammonium tetroxalate dihydrate, Acta Cryst. A 28 (1972), 522−527.

[57] W. Li, M. R. Probert, M. Kosa, M., T. D. Bennett, A, Thirumurugan, R. P. Burwood, M. Parinello, J. A. Howard, A. K. Cheetham, Negative linear compressibility of a metal−organic framework, J. Am. Chem. Soc. 134 (2012) 11940−11943.

[58] P. Hohenberg, W. Kohn, Inhomogeneous electron gas, Phys. Rev. 136 (1964) B864–B871.

[59] W. Kohn, L. J. Sham, Self-consistent equations including exchange and correlation effects, Phys. Rev. 140 (1965) A1133–A1138.

[60] R. G. Parr, W. Yang, Density-Functional Theory of Atoms and Molecules, Oxford University Press, New York, 1989.

[61] M. C. Payne, M. P. Teter, D. C. Ailan, A. Arias, J. D. Joannopoulos, Iterative minimization techniques for ab initio total-energy calculations: molecular dynamics and conjugate gradients, Rev. Mod. Phys. 64 (1992) 1045–1097.

[62] L. J. Bonales, F. Colmenero, J. Cobos, V. Timón, Spectroscopic Raman characterization of rutherfordine: combined DFT and experimental study, Phys. Chem. Chem. Phys. 18 (2016) 16575–16584.

[63] F. Colmenero, L. J. Bonales, J. Cobos, V. Timón, Study of the thermal stability of studtite by in situ Raman spectroscopy and DFT calculations, Spectrochim. Acta. A 174 (2017) 245–253.

[64] F. Colmenero, L. J. Bonales J. Cobos and V. Timón, Thermodynamic and mechanical properties of rutherfordine mineral based on density functional theory. J. Phys. Chem. C 121 (2017) 5994−6001.

[65] F. Colmenero, L. J. Bonales, J. Cobos and V. Timón, Structural, mechanical and vibrational study of uranyl silicate mineral soddyite by DFT calculations, J. Solid State Chem. 253 (2017) 249−257.

[66] F. Colmenero, L. J. Bonales, J. Cobos and V. Timón, Density functional theory study of the thermodynamic and Raman vibrational properties of $\gamma - UO_3$ polymorph, J. Phys. Chem. C 121 (2017) 14507−14516.

[67] F. Colmenero, L. J. Bonales, J. Cobos, V. Timón, Structural, mechanical and Raman spectroscopic characterization of layered uranyl silicate mineral uranophane-α by DFT methods, Clay Miner. (2018); DOI: 10.1180/clm.2018.27.

[68] F. Colmenero, J. Cobos, V. Timón, Periodic density functional study of the structure, Raman spectrum and mechanical properties of schoepite mineral, Inorg. Chem. 57 (2018) 4470−4481.

[69] F. Colmenero, A. M. Fernández, J. Cobos, V. Timón, Periodic DFT study of the thermodynamic properties and stability of schoepite and metaschoepite mineral phases, ACS Earth Space. Chem. (2018); under review.

[70] F. Colmenero, A. M. Fernández, J. Cobos, V. Timón, Thermodynamic properties of uranyl containing materials based on density functional theory, J. Phys. Chem. C 122 (2018) 5254–5267.

[71] F. Colmenero, A. M. Fernández, J. Cobos, V. Timón, Temperature dependent free energies of reaction of uranyl containing materials based on density functional theory, J. Phys. Chem. C 122 (2018) 5268–5279.

[72] F. Colmenero, A. M. Fernández, J. Cobos, V. Timón, Becquerelite mineral phase: crystal structure and thermodynamic and mechanic stability by using periodic DFT, RSC Adv. 8 (2018) 24599–24616.

[73] J. P. Perdew, K. Burke, M. Ernzerhof, Generalized gradient approximation made simple, Phys. Rev. Lett. 77 (1996) 3865–3868.

[74] S. Grimme, Semiempirical GGA-type density functional constructed with a long-range dispersion correction, J. Comput. Chem. 27 (2006) 1787–1799.

[75] S. J. Clark, M. D. Segall, C. J. Pickard, P. J. Hasnip, M. I. J. Probert, K. Refson, M. C. Payne, First principles methods using CASTEP, Z. Kristallogr. 220 (2005) 567–570.

[76] V. Milman, K. Refson, S. J. Clark, C. J. Pickard, J. R. Yates, S.-P. Gao, P. J. Hasnip, M. I. J. Probert, A. Perlov, M. D. Segall, Electron and vibrational spectroscopies using DFT, plane waves and pseudopotentials: CASTEP implementation, J. Mol. Struct. THEOCHEM 954 (2010) 22–35.

[77] MaterialsStudio, http://accelrys.com/products/collaborativescience/biovia-materials-studio/, accessed March 30, 2018.

[78] N. Troullier, J. L. Martins, Efficient pseudopotentials for plane-wave calculations, Phys. Rev. B 43 (1991) 1993–2006.

[79] B. G. Pfrommer, M. Cote, S. G. Louie, M. L. Cohen, Relaxation of crystals with the quasi-Newton method, J. Comput. Phys. 131 (1997) 233–240.

[80] H. J. Monkhorst, J. D. Pack, Special points for Brillouin-zone integration, Phys. Rev. B 13 (1976) 5188–5192.

[81] R. T. Downs, K. L. Bartelmehs, G. V. Gibbs, M. B. Boisen, Interactive software for calculating and displaying X-ray or neutron powder diffractometer patterns of crystalline materials, Am. Mineral. 78 (1993) 1104–1107.

[82] S. Baroni, S. de Gironcoli, A. Dal Corso, Phonons and related crystal properties from density-functional perturbation theory, Rev. Mod. Phys. 73 (2001) 515–562.

[83] S. Baroni, P. Giannozzi, A. Testa, Green's-function approach to linear response in solids, Phys. Rev. Lett. 58 (1987) 1861–1864.

[84] X. Gonze, D. C. Allan, M. P. Teter, Dielectric tensor, effective charges and phonon in α-quartz by variational density-functional perturbation theory, Phys. Rev. Lett. 68 (1992) 3603–3606.

[85] X. Gonze, C. Lee, Dynamical matrices, Born effective charges, dielectric permittivity tensors, and interatomic force constants from density-functional perturbation theory, Phys. Rev. B 55 (1997) 10355–10368.

[86] K. Refson, P. R. Tulip, S. J. Clark, Variational density-functional perturbation theory for dielectrics and lattice dynamics, Phys. Rev. B 73 (2006) 155114.

[87] W. J. Hehre, L. Radom, P. V. R. Schleyer, J. A. Pople, Ab Initio Molecular Orbital Theory, Wiley, New York, 1986.

[88] C. Lee, X. Gonze, Ab initio calculation of the thermodynamic properties and atomic temperature factors of SiO_2 α-quartz and stishovite, Phys. Rev. B 51 (1995) 8610–8613.

[89] J. D. Martin, XPowder12, Ver. 04.13, 2012.

[90] The International Center for Diffraction Data; PDF-2 Database, 2003; http://www.icdd.com/products/pdf2.htm (accessed March 30, 2018).

[91] D. L. Gray and A. G. Robiette, The anharmonic force field and equilibrium structure of methane, Mol. Phys. 37 (1979) 1901−1920.

[92] K. Nakamoto, Infrared and Raman Spectra of Inorganic and Coordination Compounds, J. Wiley and Sons, New York, 1986.

[93] B. L. Berg, E. A. Cloutis, P. Beck, P. Vernazza, J. L. Bishop, D. Takir, V. Reddy, D. Applin, P. Mann, Reflectance spectroscopy (0.35–8 μm) of ammonium-bearing minerals and qualitative comparison to Ceres-like asteroids, Icarus 265 (2016) 218–237.

[94] S. Satoh, T. Sogabe, The specific heats of some solid aliphatic acids and their ammonium salts and the atomic heat of nitrogen, Sci. Pap. Inst. Phys. Chem. Res. (Tokyo) 36 (1939) 97–105.

[95] E. S. Domalsky, E. D. Hearing, Heat capacities and entropies of organic compounds in the condensed phase. Volume III, J. Phys. Chem. Ref. Data 25 (1996) 1–523.

[96] J. D. Cox, D. D. Wagman, V. A. Medvedev, CODATA Key Values for Thermodynamics, Hemisphere Publishing Corp., New York, 1989.

[97] D. D. Wagman, W. H. Evans, V. B. Parker, R. H. Schumm, I. Halow, *et al.*, The NBS Tables of Chemical Thermodynamic Properties. Selected Values for Inorganic and C1 and C2 Organic Substances in SI Units, J. Phys. Chem. Ref. Data 11 Suppl. 2 (1992) 1–392.

[98] M. W. Chase, C. A. Davies, J. R. Downey, D. J. Frurip, R. A. McDonald, A. N. Syverud, JANAF Thermochemical Tables. Third Edition, J. Phys. Chem. Ref. Data 14 Suppl. 1 (1985) 1–1856.

[99] M. N. Radhahrishnan Nair, V. R. Verneker, Incomplete decomposition of ammonium oxalate, Combustion and Flame 25 (1975) 301–307.

[100] P. Pazapian, J. Pizzolato, J. A. Patrick, Thermal decomposition of oxalates of ammonium and potassium, J. Am. Ceram. Soc. 54 (1971) 250−254.

[101] L. Erdey, S. Gal, G. Liptay, Thermoanalytical properties of grade reagents. Ammonium salts, Talanta 11 (1964) 913–940.

[102] R. L. Frost, M. L. Weier, The ‘cave’ mineral oxammite – a high resolution thermogravimetry and Raman spectroscopic study, Neues Jahrbuch fuer Mineralogie - Monatshefte (2004), 27–48.